# Estimation of energy pumping time in bistable NES and experimental validation

Zhenhang Wu, Sébastien Seguy, Manuel Paredes

# Estimation of energy pumping time in bistable NES and experimental validation

**Zhenhang Wu**
Institut Clément Ader (ICA), CNRS,
INSA-ISAE-Mines Albi-UPS,
Université de Toulouse,
3 rue Caroline Aigle
Toulouse, F-31400, France
zhenhang.wu@insa-toulouse.fr

**Sébastien Seguy**
Institut Clément Ader (ICA), CNRS,
INSA-ISAE-Mines Albi-UPS,
Université de Toulouse,
3 rue Caroline Aigle
Toulouse, F-31400, France
sebastien.seguy@insa-toulouse.fr

**Manuel Paredes**
Institut Clément Ader (ICA), CNRS,
INSA-ISAE-Mines Albi-UPS,
Université de Toulouse,
3 rue Caroline Aigle
Toulouse, F-31400, France
manuel.paredes@insa-toulouse.fr

The bistable Nonlinear Energy Sink (NES) shows high efficiency in mitigating vibration through Targeted Energy Transfer (TET). It performs well in low and high energy input cases, whereas, for a cubic NES, TET occurs only above a certain energy threshold. In this work, the measure of energy pumping time is extended to a harmonic excitation case by the application of a particular integration assumption. An equivalent point in the Slow Invariant Manifold (SIM) structure can represent the average variation of the amplitudes of LO and NES. The marked robustness of this semi-analytical prediction method under parameter perturbation is investigated numerically here. The influence of parameters on the rate at which the amplitude declines is also investigated for both impulsive and harmonic excitation. The pumping time estimation is validated in a low energy input experimental test.

## 1 Introduction

In the last two decades, a novel absorber attached to the primary system by a nonlinear component has shown good performance in efficiently dissipating energy [1]. This type of nonlinear absorber, named the Nonlinear Energy Sink (NES), has been the object of much attention to explore its potential in vibration mitigation [2, 3] and energy harvesting [4, 5].

The conventional Tuned Mass Damper (TMD), where the additional mass is fixed to the primary system by linear springs and damping, has a fixed, narrow absorption frequency. When the external excitation moves away from its natural frequency or when a disturbance occurs, the TMD absorbs energy significantly less efficiently. The NES possesses a more comprehensive range of absorption frequencies than the TMD, and the risk of a resonance peak can also be avoided thanks to its adaptive stiffness [6]. Nonconstant stiffness indicates that the NES is insensitive to stiffness degradation and is thus robust with respect to changes in the underlying structure [7]. The mass of a TMD is about 10 % of the principal mass, while the mass of a NES can represent 1 % of the the principal mass and still maintain good absorbing performance [8].

One of the distinctive characteristics of the NES is the Targeted Energy Transfer (TET), where the energy of the primary system is transferred into the NES and dissipated passively by damping. There is a threshold energy input to activate this highly efficient energy dissipation procedure [9]. The energy pumping phenomenon occurs in the vicinity of 1:1 resonance, which means that the Linear Oscillator (LO) and the NES oscillate at the same frequency. If harmonic excitation imposes the primary system, it gives rise to a relaxation-type of oscillation. This kind of Strongly Modulated Response (SMR) is determined by the Slow Invariant Manifold (SIM), which is independent of the energy input. This kind of motion is not related to the SIM fixed points; the phase trajectory of the instant amplitude of LO and NES moves along the SIM. When the slow flow arrives at the singularity point, it crosses the unstable region, jumps to the stable branch, and then slides down or climbs up along the right stable branch. Gendelman describes the necessary condition for the SMR, and the threshold of excitation ampli-

tude for the existence of fold singularities to be obtained on the lower and upper fold [10]. The stability of the SMR has been transformed into a 1-D mapping problem to make the phase trajectory return to a certain interval [11].

The effect of TET and the feasibility of NES has been achieved by various experimental implementations [12, 13]. McFarland used a thin rod (piano wire) with no pretension to produce a cubic nonlinearity. The LO and NES can move along the air track [14]. In an acoustic system, the targeted energy transfer also appears between the acoustic medium and the visco-elastic membrane [9].

SIM is an efficient, fundamental tool to describe the relationship between NES and LO. Every point in the SIM structure represents one periodic solution for a certain energy level. So to obtain the SIM, the Multiple Scales Method (MSM) expands the real-time t, into multiple and independent time scales $\tau_0 = t, \tau_1 = \varepsilon\tau_0, ...$ [15]. The MSM is always accompanied by the introduction of Manevitch variables [16]. Manevitch variables offer the tool to separate the slow variant amplitude information and fast oscillation component. This method is also known as CompleXification-Averaging (CX-A).

According to the source of nonlinearity, the NES can be classified as a cubic NES, bistable NES [17, 18], Vibro-Impact (VI) NES [19–21], track NES [22], lever-type NES [23], piecewise NES [24] and rotary NES [25,26]. In a rotary NES, the rotator mass can rotate with any primary system frequency, which is totally different from what occurs with conventional mechanically constructed nonlinearity. However, the TET only exists in the rotational stage, as validated by both numerical and experimental methods [27]. The VI NES contains a ball that can move freely inside the clearance and dissipates its excessive energy through consecutive impacts [19]. The bistable NES introduces the two equilibria, one on either side, and the negative stiffness offers a higher absorbing efficiency limitation than the same cubic NES case [28]. In the presentation of negative stiffness, the response regimes under various energy levels are more complex than in the cubic NES case, especially the chaos behaviours. The two pre-stretched springs can also achieve the bistable NES. The various behaviors of multiple symmetrical and unsymmetrical in and out of phase backbone under the effect of varying pre-compression length ratio, varying stiffness are analysed through frequency–energy plots [29]. A higher order of Taylor series expansion to describe the accurate nonlinear force is addressed. The wavelet frequency spectrum confirms bistable NES scatters energy at different frequency levels through multiple resonance captures. Generally, an intra-well oscillation, inter-well oscillations with chaotic motion, SMR and stable periodic response occur sequentially as the energy increases [30]. If the negative stiffness is optimized, the bistable NES can also possess high efficiency in the low energy cases, which cubic NES hardly ever achieves. The occurrence of chaos always results from the global homoclinic bifurcation, and the Melnikov analysis provides an approximate criterion to predict the chaos regime. Based on that, the parameter boundary of chaos in bistable NES [28,31] and the relative performance of various kinds of NES is verified [32].

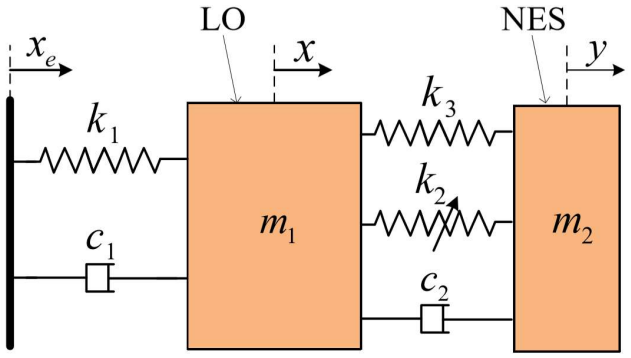


Fig. 1. Diagram of bistable NES system

The method to measure the energy decay rate was established [33, 34] for the transient response case. However, further adaptation is required to expand its application to a harmonic force case, which is addressed in this work. This study is structured as follows. In the second section, the MSM and CX-A method is used to derive the slow flow dynamics. The algebraic formulas measure the energy pumping time for both impulsive excitation and harmonic excitation. In the third section, a particular assumption is applied to obtain the expression of energy pumping time for harmonic excitation for every single SMR cycle. The robustness of this technique is verified numerically under the influence of parameters. In the fourth section, an experimental implementation is carried out. The last section mentions some remarkable conclusions.

## 2 Model analysis processing

The NES consists of a relatively light additional mass $m_2$, connected to the main system $m_1$ by negative stiffness $k_3$, cubic nonlinearity value $k_2$ and linear damping $c_2$ (Fig. 1). When harmonic excitation $x_e = Gcos(\omega t)$ is imposed on the primary system mass $m_1$ by means of linear springs $k_1$ and linear damping $c_1$, the vibration energy flows to the NES and is finally dissipated. The equation that describes the system is as follows:

$$\begin{aligned} &m_1\ddot{x} + k_1 x + c_1\dot{x} + c_2(\dot{x}-\dot{y}) \\ &+k_2(x-y)^3 + k_3(x-y) = k_1 x_e + c_1\dot{x}_e \\ &m_2\ddot{y} + c_2(\dot{y}-\dot{x}) + k_2(y-x)^3 + k_3(y-x) = 0 \end{aligned} \tag{1}$$

By introducing the rescaled variables (2) and substituting the new variable $v = x + \varepsilon y$ and $w = x - y$, the corresponding dimensionless equation is expressed in Eqn. (3). $v$ and $w$ represent the displacement of mass and the relative displacement of the bistable NES, respectively.

$$\begin{aligned}
&\varepsilon = \frac{m_2}{m_1}, \omega_0^2 = \frac{k_1}{m_1} \\
&K = \frac{k_2}{m_2\omega_0^2}, \delta = \frac{k_3}{m_2\omega_0^2}, \lambda_1 = \frac{c_1}{m_2\omega_0} \\
&\lambda_2 = \frac{c_2}{m_2\omega_0}, F = \frac{G}{\varepsilon}, \Omega = \frac{\omega}{\omega_0}, \tau = \omega_0 t
\end{aligned} \tag{2}$$

$$\begin{aligned}
&\ddot{v} + \varepsilon\lambda_1 \frac{\dot{v}+\varepsilon\dot{w}}{1+\varepsilon} + \frac{v+\varepsilon w}{1+\varepsilon} = \varepsilon F\cos\Omega\tau \\
&\ddot{w} + \varepsilon\lambda_1 \frac{\dot{v}+\varepsilon\dot{w}}{1+\varepsilon} + \frac{v+\varepsilon w}{1+\varepsilon} + \lambda_2(1+\varepsilon)\dot{w} \\
&+K(1+\varepsilon)w^3 + \delta(1+\varepsilon)w = \varepsilon F\cos\Omega t
\end{aligned} \tag{3}$$

The study is based on the fact that LO and NES vibrate at the same frequency, $\Omega$, which refers to 1:1 resonance capture. The complex averaging method is applied to Eqn. (3) by introducing the following variables (4), with $i$ the imaginary unit to investigate the analytical behaviours in the vicinity of its natural frequency. $\phi_1(\tau)$ and $\phi_2(\tau)$ modulate the amplitude of both LO and NES.

$$\begin{aligned}
\phi_1(\tau)e^{i\Omega\tau} &= \frac{d}{d\tau}v(\tau) + i\Omega v(\tau) \\
\phi_2(\tau)e^{i\Omega\tau} &= \frac{d}{d\tau}w(\tau) + i\Omega w(\tau)
\end{aligned} \tag{4}$$

The complex variables will result in secular terms containing the different powers of $e$ and only terms with $e^{i\Omega\tau}$ are conserved. So the slowly modulated system is obtained in Eqn. (5).

$$\begin{aligned}
&\dot{\phi}_1 + \frac{i\Omega}{2}\phi_1 + \frac{\varepsilon\lambda_1(\phi_1+\varepsilon\phi_2)}{2(1+\varepsilon)} - \frac{i(\phi_1+\varepsilon\phi_2)}{2\Omega(1+\varepsilon)} - \frac{\varepsilon F}{2} = 0 \\
&\dot{\phi}_2 + \frac{i\Omega}{2}\phi_2 + \frac{\varepsilon\lambda_1(\phi_1+\varepsilon\phi_2)}{2(1+\varepsilon)} - \frac{i(\phi_1+\varepsilon\phi_2)}{2\Omega(1+\varepsilon)} - \frac{\varepsilon F}{2} \\
&+\frac{\lambda_2(1+\varepsilon)\phi_2}{2} \quad - \frac{3iK(1+\varepsilon)\phi_2^2\phi_2}{8\Omega^3} - \frac{i\phi_2\delta(1+\varepsilon)}{2\Omega} = 0
\end{aligned} \tag{5}$$

In the actual dynamics, the variation of the amplitude is much slower than the rapid oscillation, the system is assumed to contain different time scales and is expressed as $\phi_i = \phi_i(\tau_0, \tau_1, \ldots)$, where the fast time scale is $\tau_0 = \tau$ and the slow time scale is $\tau_1 = \varepsilon\tau$. Under this assumption, the derivation is developed with respect to various time scales $\frac{d}{d\tau} = \frac{\partial}{\partial\tau_0} + \varepsilon\frac{\partial}{\partial\tau_1} + \cdots$.

In the context of our study, $\Omega$ is in the vicinity of 1, a detuning parameter $\sigma$ is added to represent the reduced natural frequency of OL ($\Omega = 1 + \varepsilon\sigma$) and the small parameter $\varepsilon \approx 0.01$; the terms containing higher powers of $\varepsilon$ are omitted. When the complex variables method is applied and the $\varepsilon^0$ terms and $\varepsilon^1$ terms are collected together, it follows that:

Order $\varepsilon^0$:

$$\begin{aligned}
&\frac{d}{d\tau_0}\phi_1 = 0 \\
&\frac{d}{d\tau_0}\phi_2 + \frac{1}{2}i(\phi_2-\phi_1) + \frac{1}{2}\phi_2\lambda_2 - \frac{3}{8}iK\phi_2^2\bar{\phi}_2 - \frac{1}{2}i\delta\phi_2 = 0
\end{aligned} \tag{6}$$

Order $\varepsilon^1$:

$$\begin{aligned}
&\frac{d}{d\tau_1}\phi_1 + \frac{1}{2}\lambda_1\phi_1 + \frac{1}{2}i(\phi_1-\phi_2) + i\sigma\phi_1 - \frac{1}{2}F = 0 \\
&\frac{d}{d\tau_1}\phi_2 + \frac{1}{2}\lambda_1\phi_1 + \frac{1}{2}\phi_2\lambda_2 + \frac{1}{2}i\sigma(\phi_1+\phi_2) - \frac{1}{2}F \\
&+\frac{1}{2}i(\phi_1-\phi_2) - \frac{3}{8}iK(1-3\sigma)\phi_2^2\bar{\phi}_2 + \frac{1}{2}i\delta(\sigma-1)\phi_2 = 0
\end{aligned} \tag{7}$$

### 2.1 Estimation of energy pumping time

The first equation in Eqn. (6) indicates that the $\phi_1$ is independent of the $\tau_0$ time scale. It can be demonstrated that $\phi_1$ and $\phi_2$ evolve toward an equilibrium state for $\tau_0 \to \infty$. Setting the derivative with respect to $\tau_0$, the first equation in Eqn. (7) and the second equation in Eqn. (6) yield:

$$\begin{aligned}
&\frac{1}{2}i(\phi_2-\phi_1) + \frac{1}{2}\phi_2\lambda_2 - \frac{3}{8}iK\phi_2^2\bar{\phi}_2 - \frac{1}{2}i\delta\phi_2 = 0 \\
&\frac{\mathrm{d}}{\mathrm{d}\tau_1}\phi_1 + \frac{1}{2}\lambda_1\phi_1 + \frac{1}{2}i(\phi_1-\phi_2) + i\sigma\phi_1 - \frac{1}{2}F = 0
\end{aligned} \tag{8}$$

The complex variables with polar notation $\phi_1(\tau_1) = R_1(\tau_1)e^{i\delta_1(\tau_1)}$, $\phi_2(\tau_1) = R_2(\tau_1)e^{i\delta_2(\tau_1)}$ and $\overline{\phi_2}(\tau_1) = R_2(\tau_1)e^{-i\delta_2(\tau_1)}$ are substituted in Eqn. (8). $R_1$ and $R_2$ modulate the amplitude envelope of LO and NES. By separating the real and imaginary terms, the following set of equations Eqn. (9) is obtained after simple algebraic manipulation.

$$\begin{aligned}
&\frac{2\partial R_1}{\partial T_1} - R_2\sin(\delta_1-\delta_2) + \lambda_1 R_1 - \cos(\delta_1)F = 0 \\
&2R_1\frac{\partial\delta_1}{\partial T_1} + R_1 - R_2\cos(\delta_1-\delta_2) + 2\sigma R_1 + \sin(\delta_1)F = 0 \\
&(1-\delta-\frac{3}{4}KR_2^2)R_2\sin(\delta_1-\delta_2) + \lambda_2\cos(\delta_1-\delta_2) = 0 \\
&R_1 + (\frac{3}{4}KR_2^2 + \delta - 1)R_2\cos(\delta_1-\delta_2) + R_2\lambda_2\sin(\delta_1-\delta_2) = 0
\end{aligned} \tag{9}$$

Resolving the third and fourth equation in Eqn. (9), the expression of $\cos(\delta_1-\delta_2)$ and $\sin(\delta_1-\delta_2)$ can be expressed as

$$\begin{aligned}
\cos(\delta_1-\delta_2) &= -\frac{4(3KR_2^2+4\delta-4)R_1}{R_2((3KZ_2+4\delta-4)^2+16\lambda_2^2)} \\
\sin(\delta_1-\delta_2) &= -\frac{16\lambda_2 R_1}{R_2((3KZ_2+4\delta-4)^2+16\lambda_2^2)}
\end{aligned} \tag{10}$$

The above expression satisfies the relation $cos(x)^2 + sin(x)^2 = 1$ and shows an intrinsic property of bistable NES

system. Substituting (10) into the first two equations in (9), the variation of LO amplitude is presented as follows in Eqn. (11), with $Z_1 = R_1^2$ and $Z_2 = R_2^2$.

$$\begin{aligned} Z_1 &= Z_2((\delta + \frac{3}{4}KZ_2 - 1)^2 + \lambda_2^2) \\ \frac{\partial}{\partial \tau_1} Z_1(\tau_1) &= -\lambda_2 Z_2 - \lambda_1 Z_1 + R_1 \cos(\delta_1) F \end{aligned} \tag{11}$$

The first equation of Eqn. (11) is also known as the Slow Invariant Manifold (SIM). Every point in the SIM branch indicates a potential steady response solution, the stability of which can be determined by applying the perturbation method and observing whether the roots of its characteristic equation lie on the left half of the complex plane.

The right-hand side of the second equation of Eqn. (11) indicates that the amplitude of LO is naturally decreasing because its derivation is always negative if there is no external force (F = 0). A Hamiltonian system indicates that $Z_1$ has a derivative of zero and the amplitude of LO remains constant. It results in the energy exchange without dissipation in the Hamiltonian system. The targeted energy transfer from LO is an inherent property of the system in the presence of damping. With the existence of the term $\cos(\delta_1)F$, whose positivity or negativity is not fixed, the derivative of $Z_1$ can be positive. This gives rise to a relaxation-type oscillation.

### 2.2 Energy pumping time for transient response

For the sake of simplicity, the response of transient excitation (F = 0, $\dot{v}(0) \neq 0$) is considered first. In this case, the right-hand side of the second equation of Eqn. (11) is always negative, and the energy localized in LO decreases continuously. The derivation of $Z_2$ with respect to $\tau_1$ is obtained by deriving the SIM with respect to $Z_2$ and then combining it with the second equation of Eqn. (11).

$$\frac{\partial}{\partial \tau_1} Z_2 = \frac{-\lambda_1 Z_1 - \lambda_2 Z_2}{\frac{27}{16}K^2 Z_2^2 + 3KZ_2(\delta - 1) + (\delta - 1)^2 + \lambda_2^2} \tag{12}$$

It is difficult to separate the variables and integrate the Eqn. (12). However, if the damping of the primary system is not considered ($\lambda_1$ = 0), the separation of variables leads to a possible integration, as follows:

$$\begin{aligned} C + \lambda_2 \tau_1 &= \frac{27}{32}K^2 Z_2^2 + 3KZ_2(\delta - 1) + \ln(Z_2)\left((\delta - 1)^2 + \lambda_2^2\right) \\ \lambda_1 \tau_{1,p} &= I(Z_2(1)) - I(Z_2(0)) \end{aligned} \tag{13}$$

The right-hand side of the first equation of Eqn. (13) is marked as $I(Z_2)$, describing the state of the systems. When the initial $Z_2(0)$ decreases to $Z_2(1)$, the slow time interval, $\tau_{1,p}$, of this process can be obtained by calculating the state variables $I(Z_2(0))$ and $I(Z_2(1))$ from initial state to end state. This process is visualized with the red dashed line in the SIM structure in Fig. 2.

For the condition that $\lambda_1 \neq 0$, the pumping time $\tau_{1,p}$ from initial state and end state can be solved according to the following equation.

$$\begin{aligned} &\int_0^{\tau_{1,p}} (-\frac{9}{16}\lambda_1 K^2 Z_2^2 + \frac{3}{2}\lambda_1 K(1 - \delta)Z_2) d\tau_1 \\ &-(\lambda_1(1 - \delta)^2 + \lambda_1\lambda_2^2 + \lambda_2)\tau_1 = I(Z_2(0)) - I(Z_2(1)) \end{aligned} \tag{14}$$

While the trajectory descends from $Z_2(0)$ to $Z_2(1)$, $Z_2$ is the function of $\tau_1$, which is hard to express in an explicit form. However, $Z_2$, which represents the amplitude of NES, is almost constant. This assumption that $Z_2$ remains constant during the TET has been verified numerically [33]. So, in the integration term in Eqn. (14), $Z_2$ is assumed to be a constant $Z_{2,c}$. $Z_{2,c}$ measures the average value of $Z_2$ during TET. It is determined by slow flow dynamics in the undamped condition $\lambda_1 = 0$.

$$\begin{aligned} Z_{2,c} &= \frac{\int_0^{\tau_1} Z_2 d\tau_1}{\tau_{1,p}} \\ &= \frac{\int_{Z_2(1)}^{Z_2(0)} (\frac{27}{16}K^2 Z_2^2 + 3KZ_2(\delta - 1) + (\delta - 1)^2 + \lambda_2^2) dZ_2}{\lambda_2 \tau_{1,p}} \\ &= \frac{[\frac{9}{16}K^2(Z_2^3) + \frac{3}{2}K(\delta - 1)(Z_2^2) + (\delta - 1)^2 Z_2 + \lambda_2^2(Z_2)]|_{Z_2(1)}^{Z_2(0)}}{\lambda_2 \tau_{1,p}} \end{aligned} \tag{15}$$

Finally, the energy pumping time $\tau_{1,p}$ between two states from $Z_2(0)$ to $Z_2(1)$ is found by solving the following equation.

$$\tau_{1,p} = \frac{I(Z_2(1)) - I(Z_2(0))}{\lambda_1(\frac{3}{4}KZ_{2,c} + \delta - 1)^2 + \lambda_1\lambda_2^2 + \lambda_2} \tag{16}$$

### 2.3 Energy pumping time for harmonic force response

The integration of second equation of Eqn. (11) involves complex terms in which the expressions for the phase $\delta_1(\tau_1)$ and the amplitude $R_1(\tau_1)$ are hard to describe analytically, when harmonic excitation F exists. It causes the integral $F\int_0^{\tau_{1,p}} R_1(\tau_1)\cos(\delta_1(\tau_1))\, d(\tau_1)$ to fail. The terms $R_1\cos(\delta_1)$ represent the real part of $\phi_1$. From an engineering interpretation point of view, $Re(\phi_1)$ is considered as amplitude information of LO. Based on this concept, an essential assumption is proposed as $R_1(\tau_1)\cos(\delta_1(\tau_1)) = \sqrt{Z_1}$. This assumption will be verified numerically in the following subsection. So the energy dissipation ratio in the harmonic force case is expressed as:

$$\frac{\partial}{\partial \tau_1} Z_2 = \frac{-\lambda_1 Z_1 - \lambda_2 Z_2 + F\sqrt{Z_1}}{\frac{27}{16}K^2 Z_2^2 + 3KZ_2(\delta - 1) + (\delta - 1)^2 + \lambda_2^2} \tag{17}$$

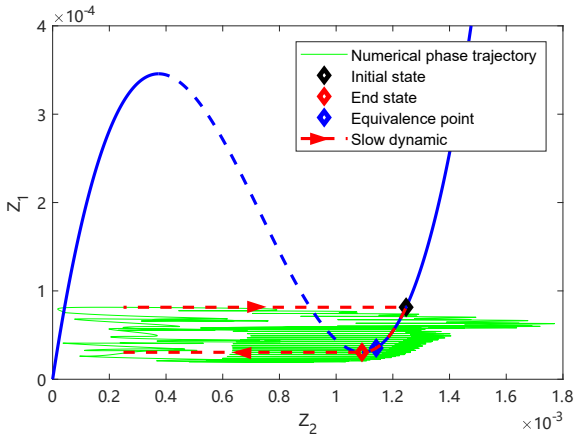


Fig. 2. The SIM structure (blue line) and transient phase trajectory (green line), which describes the descending motion from initial state to end state. The red dashed line with the arrow means the equivalent ideal slow flow motion.

Substituting the first equation of Eqn. (11), the $Z_1$ in the above equation and separating the special integrals $I(Z_2(0))$ and $I(Z_2(1))$, it gives:

$$\int_0^{\tau_{1,F}} (-\lambda_1 \frac{Z_1}{Z_2} - \lambda_2 + F\frac{\sqrt{Z_1}}{Z_2}) d\tau_1 = I(Z_2(0)) - I(Z_2(1)) \tag{18}$$

$Z_1$ can be expressed with respect to $Z_2$ according to the SIM function. This leads to failure to integrate the left side of equation Eqn. (17), if $Z_2(\tau_1)$ is treated as a time variable. However, the case of damping without force provides a simpler way to calculate this hardly-separate integral term, if $Z_2(\tau_1)$ is equal to a constant, $Z_{2,c}$. The subsequent numerical calculation results will verify the validity of this hypothesis. Although the energy pumping time of the transient response and harmonic force cases are not the same, the average value of $Z_2$ is almost identical. ($Z_{2,c}$, $Z_{1,c}$) represents the equivalent point (state) in the amplitude decline process along with the SIM. So the energy pumping time for the harmonic force case $\tau_{1,F}$ can be obtained as

$$\tau_{1,F} = \frac{Z_{2,c} I(Z_2(0)) - I(Z_2(1))}{-\lambda_1 Z_{1,c} - \lambda_2 Z_{2,c} + F\sqrt{Z_{1,c}}} \tag{19}$$

Figure. 3 is presented to better understand the calculation procedure of energy pumping time for a harmonic force case. Firstly, the parameters of the system, for example, $\varepsilon$, $\lambda_1$, $\lambda_2$, $K$ and $\delta$, are required for the determination of the geometry of the SIM. The height of initial state is chosen by the usually maximum absolute value of $Z_1$ of phase trajectory in a given SMR cycle. Meanwhile, end state is referred to as a singularity of the right stable branch of the SIM, which is already fixed in the first step. So, in the second step, the height difference is decided. $Z_{2,c}$, and special state integral terms $I(Z_2(0))$ and $I(Z_2(1))$ for the transient response case

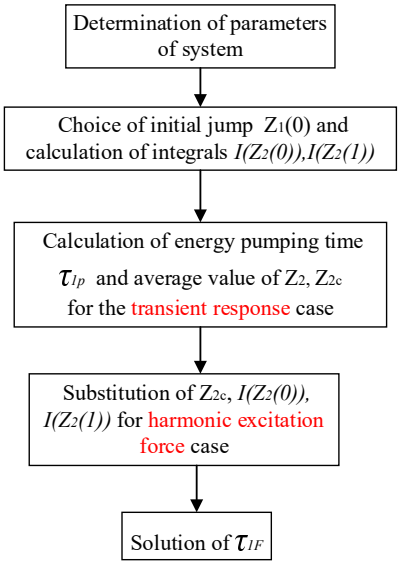


Fig. 3. Flow diagram of the calculation of energy pumping times for harmonic forces

are still the foundation of the estimation of pumping time with harmonic force in the third step. In the fourth step, the average value $Z_{2,c}$ and $Z_{1,c}$ and the other two state integrals are re-substituted into Eqn. (18) to finally solve $\tau_{1,F}$.

## 3 Robustness of semi-analytic method

### 3.1 Influence of parameters on transient response

From Eqn. (16), it is clear that the energy pumping time depends on the initial position of the right branch of the SIM. The pumping time of various energy levels was compared by both numerical and analytical methods to demonstrate the correctness of the analytical prediction. When LO is applied by various but sufficiently intensive impulse excitation, the trajectory has a snap-through motion and immediately jumps to the right stable branch of the SIM, where NES is governed by 1:1 resonance and vibrates in the vicinity of the natural frequency of LO. The initial quantitative conditions of $Z_1$ needed to trigger an efficient dissipation of energy have been discussed [35]. The influence of damping $\lambda_2$, cubic nonlinearity parameter $K$ and negative stiffness $\delta$ are considered in the following subsection in order to optimise the energy dissipation rate. The whole of the following simulation development is based on parameter sets for $\varepsilon = 0.01, \lambda_1 = 1.67, \lambda_2 = 0.167, \delta = -0.435, K = 1742$.

#### 3.1.1 Influence of initial heights

Figure. 4 presents two typical examples of energy pumping from LO to NES. The Wavelet transform (WT) results show that the dominant frequency equals the natural frequency of the LO. The NES performs 1:1 resonance occupying the whole TET period. So the energy pumping time is defined as the moment that the yellow bar disappears, which means that the trajectory crosses the saddle point in the end state $(Z_2(1), Z_1(1))$ in Fig. 2.

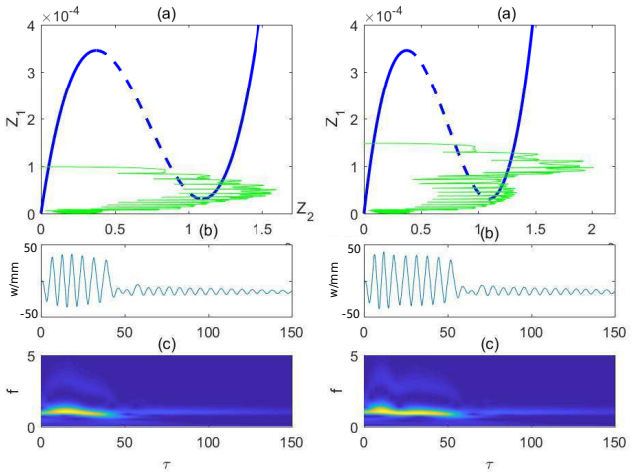


Fig. 4. TET of different input energies. Left column: $Z_1(0) = 1e-4$, right column: $Z_1(0) = 1.75e-4$ (a) phase trajectory together with SIM, (b) time-domain displacement of NES, (c) Frequency distribution of NES vibration, for $\varepsilon = 0.01, \lambda_1 = 1.67, \lambda_2 = 0.167, \delta = -0.435, K = 1742$

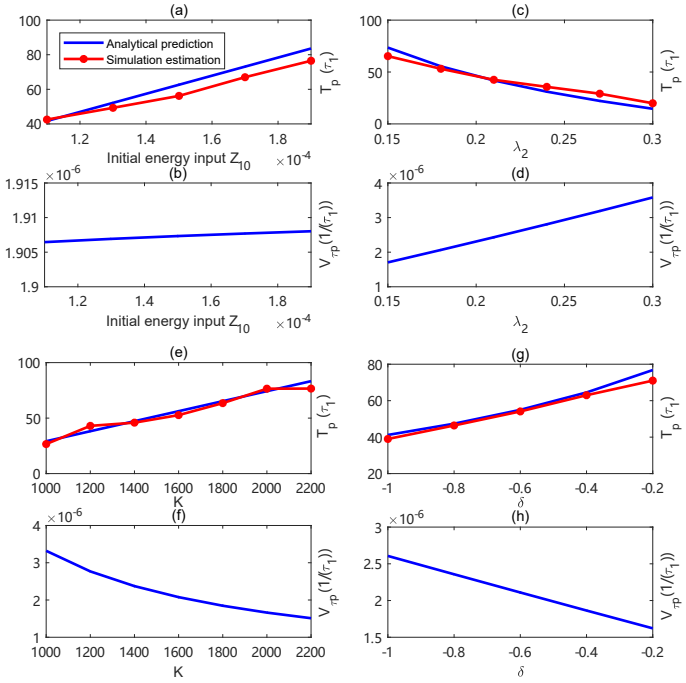


Fig. 5. Influence of parameters on the energy pumping time and the velocity of descent. (a, c, e, g) analytical prediction and simulation results, (b, d, f, h) descent rate.

Considering the variety of initial heights, a new variable is proposed to measure the velocity of descent, which is shown in Fig. 5-b. The trajectory oscillates and slips along the right branch; $V_{\tau p}$ shows the average velocity of slow flow descent.

$$V_{\tau p} = \frac{Z_1(0) - Z_1(1)}{\tau_p} \tag{20}$$

The energy pumping time found by simulation is represented by a dashed line in Fig. 5a. As the initial height increases with the end state ($(Z_2(1), Z_1(1))$ = (1.09e-3,3.052e-5) remains constant), the time that it requires for the system's trajectory to reach the saddle point at end state also rises. The relatively high energy input case simulation always gives a more significant value than the analytical prediction. The time required to descend is proportional to the height difference, which explains the phenomenon of the rate of descent remaining essentially constant for different energy inputs in Fig. 5b. Thus, it is concluded that the rate of decline of $Z_1$ is mainly determined by the system parameters and is independent of the impulsive input energy value (above the threshold energy for triggering the TET).

### 3.1.2 Influence of damping

The previous subsection briefly revealed that $\lambda_2$ has an essential impact on $V_{\tau p}$. However, the modification of $\lambda_2$ also results in a change of shape of the SIM, which is presented in Fig. 6a. An impact $Z_1(0) = 1.5e-4$ is assumed to be applied to the system so that this mid-energy maintains the error of analytical prediction at an acceptable level in different damping conditions.

As $\lambda_2$ increases, the folding point of end state, moves upwards. This implies that the system possesses a higher critical amplitude of LO when the TET disappears. The path between the initial height $Z_1(0)$ and the fold point $Z_1(1)$ decreases, which helps systems to terminate TET in a shorter time. In addition to the shortening of the path, another factor affects the duration of the TET: damping. According to Eqn. (12), a higher value of $\lambda_2$ enhances the rate of descent. With shorter paths and greater damping value, the energy pumping time is apparently reduced in Fig. 5c, and the average descent rate increases linearly with higher $\lambda_2$ in Fig. 5d.

Through the second equation of Eqn. (11), both parts, $\lambda_1 Z_1$ and $\lambda_2 Z_2$, contribute to the descent rate. When the $Z_{2,c}$ is selected, whose values are almost constant during the different descent processes, at about 1.14e-3, for the case $\lambda_2 = 0.167$. The corresponding $Z_1$ value in the SIM right branch is 3.55e-5. The different contribution of damping is calculated such that $\lambda_1 Z_1 = 0.6e-4$ and $\lambda_2 Z_2 = 1.9e-4$. The latter component mainly governs the descent rate value, because of its much larger value. To maximise the descent rate in transient response, increasing the $\lambda_2$ value can be an effective alternative. However, it also causes the LO optimal design to have a larger stable response amplitude in harmonic excitation.

### 3.1.3 Influence of stiffness

To investigate the role of cubic nonlinearity parameter $K$ and negative stiffness $\delta$, the energy pumping time and corresponding descent rate are presented in Fig. 5(e-h). The system has the same initial impact as in the previous investiga-

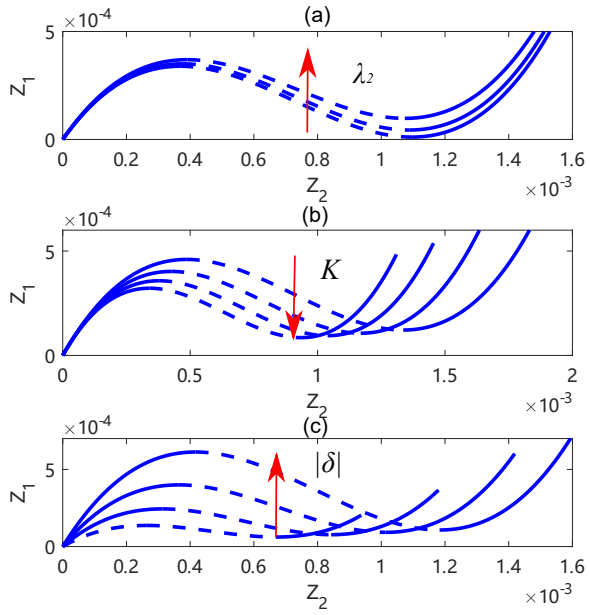


Fig. 6. Modification of SIM shape under various (a) $\lambda_2$ (0.1, 0.2, 0.3) (b) K ([1400, 1600, 1800, 2000]) (c) $\delta$ ([-0.05 -0.3 -0.55 -0.8]). Arrow indicates the case with the largest (absolute) values of corresponding parameters

tion $Z_1(0) = 1.5e-4$. Firstly, increasing the value of the cubic nonlinearity parameter and negative stiffness causes the SIM to change shape in the direction of the arrow in Fig.6b-c. The end state rises, reaching a larger value of $Z_1(1)$, which means a shorter path to cross. So the energy pumping time is longer in the case of lower nonlinear stiffness. According to the previous description, the equivalence point is located near the fold point, and an increase in K allows the fold point (or equivalence point) to have a smaller $Z_{1,c}, Z_{2,c}$. Equation. (11) indicates that the smaller $Z_{1,c}, Z_{2,c}$ values lead to a decrease in instantaneous velocity. So the decrease in average velocity with increasing K design can be explained.

When the absolute value of $\delta$ rises while the value of K remains constant, the end state, in the SIM structure moves in the direction of a higher $Z_2(1)$ value. Meanwhile, $Z_1(1)$ is almost unchanged and remains in a horizontal line while $\delta$ varies in Fig. 6c. The decrease in the average descent rate is due to the smaller $Z_2(1)$ value of the fold point. So, systems with smaller absolute $\delta$ values take a longer time to dissipate energy in Fig. 5g. The variation in the descent rate is almost linearly related to the change in $\delta$ in Fig. 5g. This feature is not the same as the quadratic decrease in decay rate as K increases. The analytical prediction shows a good fit of results in the middle interval of the $\delta$ range. In a small negative stiffness case, the analytical result is much larger than the simulated value.

It can be concluded that the variation of energy pumping time depends on the modification of the SIM shape. The rate of decline of the system is mainly due to the effect of K, $\delta$ on the position of the fold point of the SIM, which causes

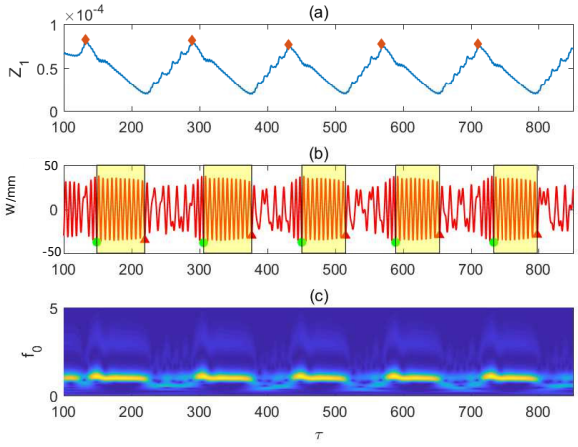


Fig. 7. Time-displacement of (a) $Z_1$, (b) w and (c) WT for w. The intervals of energy pumping time are identified and marked in yellow shaded areas

the average $Z_1, Z_2$ values to ultimately change the average velocity.

### 3.2 Influence of parameters on harmonic force response

#### 3.2.1 Various heights of initial descent

The parameters of a bistable NES for the numerical simulation are classified as modest ones. The negative stiffness introduces chaos behaviours and the snap-through motion is triggered by the chaos. The initial height at which the phase trajectory begins to descend is different and unpredictable for each complete SMR cycle. The various maximum local values of $Z_1$ are marked with the diamond dots in Fig.7a. These different $Z_1$ values are used as the initial height of descent to predict the energy pumping time for each SMR cycle.

The energy pumping process describes the energy of LO as transferred into NES and dissipated by the damping. Energy pumping is referred to as the phase trajectory descends along the righ stable branch the SIM and does not include snap-through motion. So the energy pumping time is counted from the moment the NES amplitude reaches its maximum and ends when the NES re-enters chaos. In other words, it implies a phase in which the amplitudes of LO and NES drop simultaneously. The interval of energy pumping time in each SMR cycle is identified in Fig.7b.

Based on the calculation process in the force case and initial $Z_1$ value, the predicted pumping time can be calculated, and is summarized in Tab. 1, where the unit of $Z_1(0)$ is 1e-5. $\tau_{0,a}$ are the analytical energy pumping times. $\tau_{0,s}$ are the simulated values, which are calculated by time intervals marked in Fig.7b. Each energy pumping interval starts with a green dot and ends with a red triangle. $E_r$ means the relative error between $\tau_{0,s}$ and $\tau_{0,a}$. From an intuitive point of view, a higher initial $Z_1(0)$ causes a greater distance to slide down, when the end point $Z_1(1)$ is fixed. So a longer energy pumping time is required for the same energy input level. Comparing the analysed value with the simulated value shows the analysed value to be smaller than the simulated value. An er-

Table 1. Pumping time estimation for given amplitude input G = 0.3mm

| | | | | | |
|---|---|---|---|---|---|
| $Z_1(0)$ | 8.23 | 8.15 | 7.70 | 7.73 | 7.75 |
| $\tau_{0,s}$ | 70.6 | 70.7 | 64.3 | 64.4 | 64.7 |
| $\tau_{0,a}$ | 69.4 | 68.4 | 62.6 | 62.9 | 63.2 |
| $E_r(\%)$ | 1.73 | 3.36 | 2.72 | 2.38 | 2.37 |

Table 2. Pumping time estimation for various energy inputs

| G (mm) | 0.25 | 0.275 | 0.3 | 0.325 | 0.35 |
|---|---|---|---|---|---|
| $\overline{Z_1(0)}$ | 7.23 | 8.052 | 8.04 | 8.23 | 8.075 |
| $\overline{\tau_{0,s}}$ | 39.1 | 57.35 | 68.67 | 83.42 | 109.35 |
| $\overline{\tau_{0,a}}$ | 39.8 | 55.42 | 67.02 | 87.58 | 115.56 |
| $E_r(\%)$ | -1.76 | 3.5 | 2.46 | -4.75 | -5.68 |

ror of less than 5% between the two values can be accepted. When predicting energy pumping time, this semi-analytical method is robust with respect to the uncertainty of initial height caused by chaos.

#### 3.2.2 Various energy inputs

The initial descent height of $Z_1$ for each SMR changes as time varies. So, to compare the influence of energy input level, the average $Z_1$ value was chosen within a time interval of [0,1000]($\tau$). The excitation interval was selected in the range [0.25 mm,0.35 mm] to ensure the occurrence of SMR, for which the interval of occurrence is theoretically [0.22 mm,0.44 mm].

For each excitation case, the initial height $Z_1(0)$ where each SMR starts to descend is different, as is the time it requires to descend. To calculate the average initial height, a time interval of response, which contains 5 complete SMR cycles, is selected. The upper line of $\overline{Z_1(0)}$, $\overline{\tau_{0,s}}$ and $\overline{\tau_{0,a}}$ in Tab.2 represents the average value of the corresponding parameter in these five SMR cycles. This method of calculating the mean height and the mean time was also applied in the study of the relationship between descent rate and negative stiffness.

Although the perturbation exists in the average initial height (average $Z_1(0)$ does not increase for a higher input energy in the second line of the Tab.2), the extension of the analytical and simulated pumping time shows a strong relationship with increasing excitation. Increasing the amplitude of the excitation leads both the simulated and analytical energy pumping times to show an increasing tendency in Tab.2. When the system is maintained at a low energy input, the error level is perturbed but is acceptable. However, the analytical result is larger than the simulated value in a high energy case, G = 0.35 mm. In the transient response, the high energy state also leads to a similar error distribution, i.e., a large analytical value, and a more significant excitation results in failure of the method. So low or modest energy inputs are necessary to ensure the validation of this method.

Table 3. Pumping time estimation for various negative stiffness cases for G = 0.3mm

| $k_3$(N/m) | -25 | -50 | -75 | -100 | -125 |
|---|---|---|---|---|---|
| $\overline{Z_1(0)}$ | 8.86 | 8.04 | 9.34 | 1.12 | 1.04 |
| $\overline{\tau_{0,s}}$ | 108.85 | 68.67 | 56.82 | 53.76 | 37.84 |
| $\overline{\tau_{0,a}}$ | 122.5 | 67.02 | 58.52 | 57.74 | 39.93 |
| $E_r(\%)$ | -11.1 | 2.46 | -2.9 | -6.9 | -5.23 |

#### 3.2.3 Various negative stiffness cases

Five cases with different $k_3$ values were examined further to investigate the robustness under various negative stiffness designs. Like various energy input cases, the average energy pumping times, obtained by numerical and semi-analytical methods, are compared in Tab. 3. With the variation of $\delta$, the perturbation in average initial height $Z_1(0)$ becomes more severe. As the negative stiffness declines, more time is needed to dissipate the same energy input level. In the transient response case, the larger value of $\delta$ causes the deformation of the SIM structure, where the fold point moves to a position with higher value. So the equivalent point, which is close to the fold point, has a more significant value. This variation significantly improves the decline rate, regardless of the initial height perturbation by Eqn. (11).

A bigger value of negative results in a faster dissipation ratio also leads to a larger force threshold to trigger the SMR. The analytical prediction is always larger than the simulated value. A more significant error is found in a weak bistable NES that still conserves some characteristics of a cubic NES, where the snap-through motion is triggered by crossing the singularity of SIM instead of being triggered by chaos. Those cases, with errors below 5%, are classified as modest bistable NES. This method predicts the energy pumping time more accurately in the modest bistable NES.

### 3.3 Validation of assumption

During the TET, $Z_{2,c}$ is almost constant, and it can be observed that the amplitude of NES remains constant in Fig.7 for each energy pumping period. The assumption of $R_1(\tau_1)\cos(\delta_1(\tau_1)) = \sqrt{Z_1}$ is a prerequisite for the semi-analytical method. Acquiring exact expressions of integrals is challenging, but the two sides of the equation are equivalent in the integration process. To better demonstrate this point, a numerical example for case G = 0.3 mm can provide an explanation.

When the initial maximum $Z_1(0)$ is equal to 8.15e-5, the distance in the $Z_1$ direction, between initial states and end state, $\Delta Z_1$ is -5.1e-5. The analytical energy pumping time $\tau_1 = \varepsilon\tau_0 = 0.684$. The positions of the equivalent points are

Table 4. Experimental parameters of environment

| | | | | |
|---|---|---|---|---|
| Physical | $m_1$ | $m_2$ | | |
| parameters | 5.5kg | 0.05kg | | |
| | $c_1$ | $c_2$ | $k_1$ | |
| | 5N·s/m | 0.54N·s/m | 1.15e4N/m | |
| Reduced | ε | $\lambda_1$ | $\lambda_2$ | $f_0$ |
| parameters | 0.91% | 2.18 | 0.24 | 7.27Hz |

$Z_{1,c} = 3.54e-05, Z_{2,c} = 1.14e-3$, which is close to the end state. Substituting these parameters into the second equation of (11), the average value of $R_1(\tau_1)\cos(\delta_1(\tau_1))$ during the whole TET equals 5.83e-3, while $\sqrt{Z_{1,c}}$ equals 5.95e-3. The approximation produces an error level on the integral of 2%.

Although the other parameters, for example, excitation amplitude and negative stiffness, also influence the accuracy of integral, the good agreements between simulation results and analytical predictions verify the equivalence of integrals. Thus, the following equation is valid during the energy pumping time.

$$\frac{1}{\tau_1}\int_0^{\tau_1} R_1(\tau_1)\cos(\delta_1(\tau_1))d\tau \approx \sqrt{Z_1}|_{Z_1=Z_{1,c}} \tag{21}$$

## 4 Experimental validation for estimation

A bistable nonlinearity device was constructed and is presented in Fig. 8. A linear oscillator is connected to a 10 kN electrodynamic shaker and is excited by a harmonic excitation with its natural frequency. The NES mass is embedded through a track and a four spring device. The latter provides the cubic nonlinearity and negative stiffness through adjustment of the pre-compression length of the linear spring. The two contactless displacement sensors are installed vertically to measure the absolute displacement of LO and NES. An accelerometer is also installed in the shaker to measure its acceleration. The extra digital oscilloscope and a bandpass filter can correct bias and attenuate high-frequency noise. The mass of the primary system, the NES mass and their corresponding damping are presented in Tab. 4. The dimensionless parameters (mass ratio, damping, and natural frequency) are fixed to design the optimal stiffness.

$k_0$ is the linear phase stiffness. $a_1$ and $a_3$ are the linear stiffness and cubic nonlinearity rate in the nonlinear phase of the conical spring. $l_{0l}$ and $l_c$ are the lengths of the linear spring and connector respectively. $k_l$ is the stiffness of the linear spring. By adjusting the pre-compression length $l_p$, the system can process different negative stiffnesses $k_3$ and cubic nonlinearity parameter $k_2$ to shift from the cubic NES and bistable NES. A description of the displacement-force relation is given by:

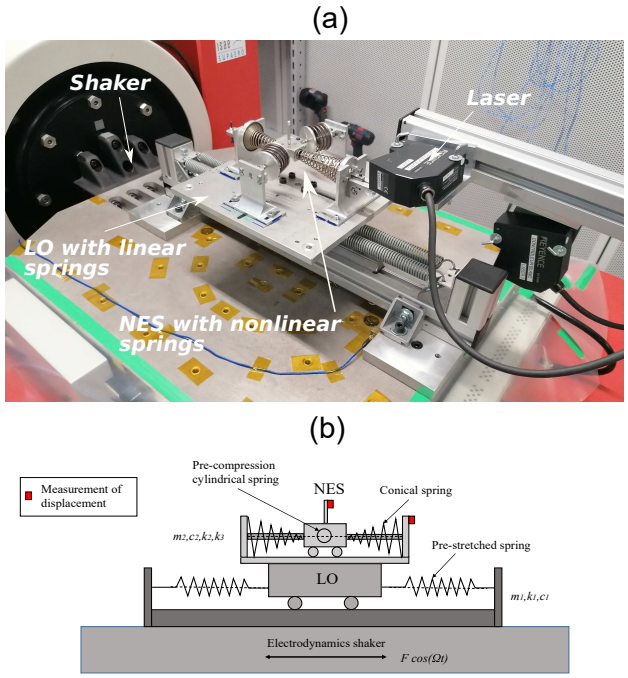


Fig. 8. (a) Detailed view of experimental setup (b) Scheme of system

Table 5. Experimental stiffness parameters of NES system

| | | | |
|---|---|---|---|
| $k_0$ | $a_1$ | $a_3$ | $k_l$ |
| 187N/m | 280N/m | 3.4e5 $N/m^3$ | 1100 N/m |
| $l_{0l}$ | $l_{p1}$ | $k_2$ | $k_3$ |
| 50 mm | 16.4 mm | 6.94e5 $N/m^3$ | -109.4 N/m |

$$\begin{aligned} F &= k_2 u + k_3 u^3 \\ k_2 &= \left(a_1 + k_0 - 2k_l \frac{l_p}{l_{0l} + 2l_c - l_p}\right) \\ k_3 &= \left(a_3 + k_l \frac{l_{0l} + 2l_c}{(l_{0l} + 2l_c - l_p)^3}\right) \end{aligned} \tag{22}$$

The linear stiffness part $k_2$ is adjusted to be zero and a cubic NES is built when the $l_p$ = 14.3 mm for the stiffness parameter, which is presented in Tab. 5.

### 4.1 Validation of estimation of energy pumping time

By compressing the pre-compression length to 16.4 mm, the parameters of the bistable characteristic are as presented in Tab. 5.The system is applied with two low excitations, G = 0.21 mm and 0.25 mm. In both cases, the bistable NES starts to perform SMR, which is presented in Fig. 9. According to the previous definition of energy pumping, which counts

Table 6. Experimental results of energy pumping time in G = 0.21 and 0.25 mm cases.

| G (mm) | 0.21 | | | | |
|---|---|---|---|---|---|
| $Z_1(0)$ | 2.80 | 3.0 | 2.76 | | |
| $t_{e,p}(s)$ | 0.44 | 0.58 | 0.44 | | |
| $t_{a,p}$ $(s)$ | 0.32 | 0.44 | 0.29 | | |
| G (mm) | 0.25 | | | | |
| $Z_1(0)$ | 2.9 | 3.44 | 3.01 | 4.7 | 2.88 |
| $t_{e,p}(s)$ | 1.02 | 1.28 | 1.00 | 1.30 | 0.86 |
| $t_{a,p}$ $(s)$ | 0.88 | 1.6 | 1.02 | 3.3 | 0.84 |

from the time the NES reaches its maximum amplitude to when the NES re-enters the chaotic state, the time instants are also marked in the figure. In the numerical simulation, the start point of $Z_1(0)$ is obtained by the time displacement of LO. However, $Z_1$ is expressed as a real part of complex variable $\phi_1(\tau)$, which cannot be recorded directly. From the perspective of a mechanical interpretation, the $Z_1$ approximately equals the square of the LO amplitude. So, the initial $Z_1(0)$ in the starting point A is selected as the square of maximum LO displacement.

The energy pumping times of both excitation cases are calculated in Tab. 6, where $t_{e,p}$ and $t_{a,p}$ are the experimental and analytical energy pumping times. In the lower energy input case, the analytical prediction time is always shorter than the experimental observation. This is also the case for the comparison with simulation, where the analytical value is always lower than the simulated one, for example, G = 0.3 mm in Tab. 1. The variation of value of the initial height $Z_1(0)$ occurs because chaos motion triggers the snap-through motion, so the maximal amplitude of LO is unpredictable and it is hard to reach the same level for each SMR cycle. The analytical prediction can estimate the energy pumping time to the same order of magnitude.

In a higher energy input case, in Fig. 9b, the initial start point also possesses a higher position than that of lower energy inputs. It also causes a need for longer pumping time to dissipate energy. The overestimation occurs in the case of initial height $Z_1(0) = 4.7e-5$. This can be considered as the failure of the analytical estimation method. In the high energy input cases of harmonic excitation, for example, G = 0.35 mm in Tab. 2, a high initial start point causes a larger error. This confirms that our analytical prediction provides a better fit for the modest energy level input. If this invalid data is excluded, the remaining mean error on the corresponding predicted values against the experiment is reduced to 4%.

## 5 Conclusion

This study focuses on the adapted method based on the SIM structure to predict the energy pumping time of a

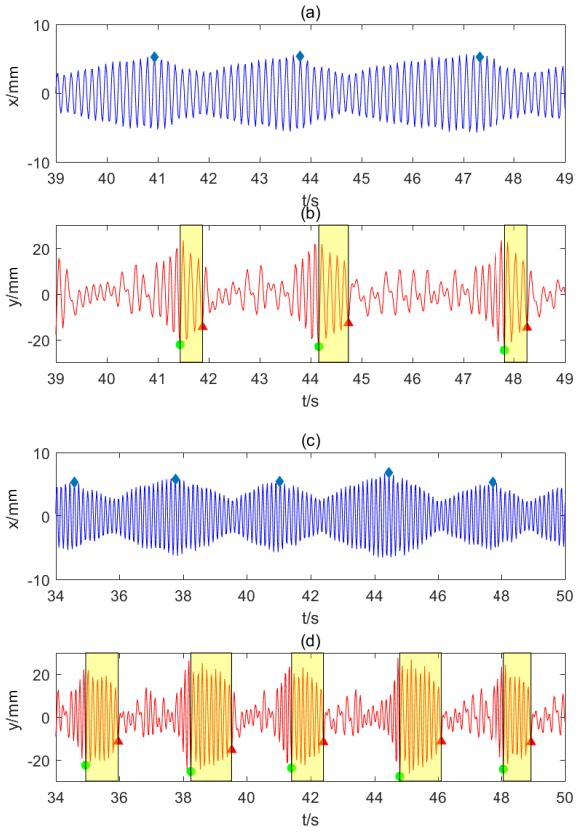


Fig. 9. Experimental time-displacement result of bistable NES and LO (a) (b) for excitation G = 0.21 mm, (c) (d) for G = 0.25 mm. The intervals of energy pumping time are identified and marked in yellow shaded areas

bistable NES under harmonic force. The calculation process has been presented to examine the robustness of prediction. The factors affecting the rate of amplitude decrease have been analysed for the transient and harmonic excitation cases. Several main conclusions can be drawn:

(1) To estimate the duration of energy pumping time in a damping and harmonic force case, the Hamiltonian system is considered first. The equivalent point, obtained by a damped, transient impulsive system, is essential for energy pumping time calculation under harmonic excitation.

(2) The influences of parameters (initial height, cubic nonlinearity parameter, negative stiffness, damping and excitation amplitude) are investigated for both transient response and harmonic force. Due to the chaos behaviours, the robustness of the semi-analytical method is tested and proved to be strong enough under parameter perturbation. A larger NES damping, lower cubic nonlinearity parameter or larger negative stiffness enhance the dissipation rate by modifying the structure of the SIM and the corresponding equivalent point position. Energy input level does not affect the LO amplitude decay rate.

(3) A particular approximation of complex integration offers the possibility to calculate the energy pumping time for every SMR cycle. Due to the chaos motion, every initial starting point is different. The numerical and experimental

results prove the robustness of the calculation method with respect to initial descent height and excitation. This prediction method shows good potential for predicting the energy pumping time at a low energy state.

## References


[1] Vakakis, A., 2001. "Inducing passive nonlinear energy sinks in vibrating systems". *J Vib Acoust,* **123**(3), pp. 324–332.

[2] Gourc, E., Seguy, S., Michon, G., Berlioz, A., and Mann, B., 2015. "Quenching chatter instability in turning process with a vibro-impact nonlinear energy sink". *Journal of Sound and Vibration,* **355**, pp. 392–406.

[3] Bergeot, B., Bellizzi, S., and Cochelin, B., 2017. "Passive suppression of helicopter ground resonance using nonlinear energy sinks attached on the helicopter blades". *Journal of Sound and Vibration,* **392**, pp. 41–55.

[4] Ahmadabadi, Z. N., and Khadem, S., 2014. "Nonlinear vibration control and energy harvesting of a beam using a nonlinear energy sink and a piezoelectric device". *Journal of Sound and Vibration,* **333**(19), pp. 4444–4457.

[5] Kremer, D., and Liu, K., 2017. "A nonlinear energy sink with an energy harvester: harmonically forced responses". *Journal of Sound and Vibration,* **410**, pp. 287–302.

[6] Gourdon, E., Alexander, N. A., Taylor, C. A., Lamarque, C.-H., and Pernot, S., 2007. "Nonlinear energy pumping under transient forcing with strongly nonlinear coupling: Theoretical and experimental results". *Journal of sound and vibration,* **300**(3-5), pp. 522–551.

[7] Tripathi, A., Grover, P., and Kalmár-Nagy, T., 2017. "On optimal performance of nonlinear energy sinks in multiple-degree-of-freedom systems". *Journal of Sound and Vibration,* **388**, pp. 272–297.

[8] Gourc, E., Michon, G., Seguy, S., and Berlioz, A., 2015. "Targeted energy transfer under harmonic forcing with a vibro-impact nonlinear energy sink: analytical and experimental developments". *J Vib Acoust,* **137**(3).

[9] Bellet, R., Cochelin, B., Herzog, P., and Mattei, P.-O., 2010. "Experimental study of targeted energy transfer from an acoustic system to a nonlinear membrane absorber". *Journal of Sound and Vibration,* **329**(14), pp. 2768–2791.

[10] Gendelman, O., Starosvetsky, Y., and Feldman, M., 2008. "Attractors of harmonically forced linear oscillator with attached nonlinear energy sink i: description of response regimes". *Nonlinear Dynamics,* **51**(1), pp. 31–46.

[11] Starosvetsky, Y., and Gendelman, O., 2008. "Strongly modulated response in forced 2dof oscillatory system with essential mass and potential asymmetry". *Physica D: Nonlinear Phenomena,* **237**(13), pp. 1719–1733.

[12] Gendelman, O., 2011. "Targeted energy transfer in systems with external and self-excitation". *Proceedings of the Institution of Mechanical Engineers, Part C: Journal of Mechanical Engineering Science,* **225**(9), pp. 2007–2043.

[13] Jiang, X., McFarland, D. M., Bergman, L. A., and Vakakis, A. F., 2003. "Steady state passive nonlinear energy pumping in coupled oscillators: theoretical and experimental results". *Nonlinear Dynamics,* **33**(1), pp. 87–102.

[14] McFarland, D. M., Kerschen, G., Kowtko, J. J., Lee, Y. S., Bergman, L. A., and Vakakis, A. F., 2005. "Experimental investigation of targeted energy transfers in strongly and nonlinearly coupled oscillators". *The Journal of the Acoustical Society of America,* **118**(2), pp. 791–799.

[15] Qiu, D., Paredes, M., and Seguy, S., 2019. "Variable pitch spring for nonlinear energy sink: Application to passive vibration control". *Proceedings of the Institution of Mechanical Engineers, Part C: Journal of Mechanical Engineering Science,* **233**(2), pp. 611–622.

[16] Manevitch, L., 2001. "The description of localized normal modes in a chain of nonlinear coupled oscillators using complex variables". *Nonlinear Dynamics,* **25**(1), pp. 95–109.

[17] Romeo, F., Manevitch, L., Bergman, L., and Vakakis, A., 2015. "Transient and chaotic low-energy transfers in a system with bistable nonlinearity". *Chaos: An Interdisciplinary Journal of Nonlinear Science,* **25**(5), p. 053109.

[18] Qiu, D., Seguy, S., and Paredes, M., 2018. "Tuned nonlinear energy sink with conical spring: design theory and sensitivity analysis". *Journal of Mechanical Design,* **140**(1), p. 011404.

[19] Li, T., Seguy, S., and Berlioz, A., 2017. "On the dynamics around targeted energy transfer for vibro-impact nonlinear energy sink". *Nonlinear Dynamics,* **87**(3), pp. 1453–1466.

[20] Qiu, D., Seguy, S., and Paredes, M., 2019. "Design criteria for optimally tuned vibro-impact nonlinear energy sink". *Journal of Sound and Vibration,* **442**, pp. 497–513.

[21] Youssef, B., and Leine, R. I., 2021. "A complete set of design rules for a vibro-impact nes based on a multiple scales approximation of a nonlinear mode". *Journal of Sound and Vibration,* **501**, p. 116043.

[22] Wang, J., Zhang, C., Li, H., and Liu, Z., 2021. "Experimental and numerical studies of a novel track bistable nonlinear energy sink with improved energy robustness for structural response mitigation". *Engineering Structures,* **237**, p. 112184.

[23] Zang, J., Cao, R.-Q., and Zhang, Y.-W., 2021. "Steady-state response of a viscoelastic beam with asymmetric elastic supports coupled to a lever-type nonlinear energy sink". *Nonlinear Dynamics,* **105**(2), pp. 1327–1341.

[24] Al-Shudeifat, M., and Saeed, A., 2022. "Periodic motion and frequency energy plots of dynamical systems coupled with piecewise nonlinear energy sink". *Journal of Computational and Nonlinear Dynamics*.

[25] Saeed, A. S., AL-Shudeifat, M. A., Vakakis, A. F., and Cantwell, W. J., 2020. "Rotary-impact nonlinear energy sink for shock mitigation: analytical and numerical investigations". *Archive of Applied Mechanics,* **90**(3), pp. 495–521.

[26] Saeed, A. S., AL-Shudeifat, M. A., and Vakakis, A. F., 2019. "Rotary-oscillatory nonlinear energy sink of robust performance". *International Journal of Non-Linear Mechanics,* **117**, p. 103249.

[27] Gendelman, O., Sigalov, G., Manevitch, L., Mane, M., Vakakis, A., and Bergman, L., 2012. "Dynamics of an eccentric rotational nonlinear energy sink". *J Appl Mech,* **79**(1).

[28] Wu, Z., Seguy, S., and Paredes, M., 2021. "Basic constraints for design optimization of cubic and bistable nes". *J Vib Acoust*, pp. 1–51.

[29] Al-Shudeifat, M. A., and Saeed, A. S., 2021. "Frequency–energy plot and targeted energy transfer analysis of coupled bistable nonlinear energy sink with linear oscillator". *Nonlinear Dynamics,* **105**(4), pp. 2877–2898.

[30] Qiu, D., Li, T., Seguy, S., and Paredes, M., 2018. "Efficient targeted energy transfer of bistable nonlinear energy sink: application to optimal design". *Nonlinear Dynamics,* **92**(2), pp. 443–461.

[31] Farshidianfar, A., and Saghafi, A., 2014. "Global bifurcation and chaos analysis in nonlinear vibration of spur gear systems". *Nonlinear Dynamics,* **75**(4), pp. 783–806.

[32] AL-Shudeifat, M. A., and Saeed, A. S., 2021. "Comparison of a modified vibro-impact nonlinear energy sink with other kinds of ness". *Meccanica,* **56**(4), pp. 735–752.

[33] Dekemele, K., De Keyser, R., and Loccufier, M., 2018. "Performance measures for targeted energy transfer and resonance capture cascading in nonlinear energy sinks". *Nonlinear Dynamics,* **93**(2), pp. 259–284.

[34] Dekemele, K., Van Torre, P., and Loccufier, M., 2019. "Performance and tuning of a chaotic bi-stable nes to mitigate transient vibrations". *Nonlinear Dynamics,* **98**(3), pp. 1831–1851.

[35] Nguyen, T. A., and Pernot, S., 2012. "Design criteria for optimally tuned nonlinear energy sinks—part 1: transient regime". *Nonlinear Dynamics,* **69**(1), pp. 1–19.